# An Extended Micromechanics Method for Probing Interphase Properties in Polymer Nanocomposites

Zeliang Liu[a], John A. Moore[b], Wing Kam Liu[c,*]

[a] *Theoretical and Applied Mechanics, Northwestern University, Evanston, IL 60208, USA*
[b] *Lawrence Livermore National Laboratory, P.O. Box 808, Livermore, CA 94551, United States*
[c] *Department of Mechanical Engineering, Northwestern University, Evanston, IL 60208, USA*

**Abstract**

Inclusions comprised on filler particles and interphase regions commonly form complex morphologies in polymer nanocomposites. Addressing these morphologies as systems of overlapping simple shapes allows for the study of dilute particles, clustered particles, and interacting interphases all in one general modeling framework. To account for the material properties in these overlapping geometries, *weighted-mean* and *additive* overlapping conditions are introduced and the corresponding inclusion-wise integral equations are formulated. An extended micromechanics method based on these overlapping conditions for linear elastic and viscoelastic heterogeneous material is then developed. An important feature of the proposed approach is that the effect of both the geometric overlapping (clustered particles) and physical overlapping (interacting interphases) on the effective properties can be distinguished. We apply the extended micromechanics method to a viscoelastic polymer nanocomposite with interphase regions, and estimate the properties and thickness of the interphase region based on experimental data for carbon-black filled styrene butadiene rubbers.

*Keywords:* Micromechanics, overlapping geometries, Boolean-Poisson model, polymer composite, viscoelasticity, interphase, inverse problem

## 1. Introduction

Nanoparticle-reinforced polymer composites have attracted intense attention in the research and industrial communities during the past decades. As the size of filler particles approaches the nano-scale, composite materials may exhibit advantageous thermal, electrical or mechanical properties, even with addition of a small amount of fillers [1, 2]. Because of these extraordinary behaviors, polymer nanocomposites also show promise as multi-functional materials in automotive and aerospace industries [3].

Many polymer fillers do not adhere to simple geometric shapes (i.e., spheres, diamonds, cylinders). Rather, fillers, such as carbon-black in tire applications, tend to have irregular geometries and to form networks of agglomerated filler particles [4]. Even, more pristine filler particle structures, such as nano-diamonds, will form larger aggregates unless explicitly processed to prevent such formation [5].

Both experiments and molecular dynamics (MD) simulations have suggested that there exists an interphase region in the vicinity of a nanoparticle, with dramatically different thermal-mechanical, mechanical and structural properties than observed in bulk polymer [6, 7, 8, 9]. For example, Cheng et al. measured the modulus of confined polymer films adjacent to a plane substrate through atomic force microscopy (AFM)-based indentation, and the thickness of the interphase is found to be around several tens of nanometers [9]. However, directly measuring mechanical properties (e.g., dynamic moduli) of the interphase in a nanoparticle-reinforced polymer composite can be challenging and/or time-consuming. In this paper, we are interested in using the overall mechanical properties of the polymer composite to inversely predict the

*Corresponding author
*Email address:* w-liu@northwestern.edu (Wing Kam Liu )

interphase properties. This motivates us to develop a general homogenization method in a natural and efficient way, that allows us to consider the shape and spacial distributions of the nanoparticles, properties of the interphase and, more importantly, the effects of overlapping regions.

Considerable effort has been put into homogenizing polymer composites with interphase regions using direct numerical simulations (DNS). Qiao et al.[3] and Peng et al.[10] used finite element (FE) methods to analyze the effects of interphase overlap and particle clustering, as well as shapes and orientations of nano-particles on the elastic and viscoelastic properties of the nanocomposite. In their FE models for nanocomposites, a representative-volume-element (RVE) is defined to be large enough to statistically represent the heterogeneous material while the overall properties are simultaneously independent of boundary conditions. Due to the resolution of a finite-element mesh needed to properly resolve strain and property gradients in the interphase, simulations on the RVE scale can become computationally expensive. Fast Fourier Transformation (FFT)-based methods [11] usually require less computational resources than FE method due to the high efficiency of existing FFT algorithms; however, the mesh in FFT-based method needs to be uniform and its convergence will be deteriorated if one material phase becomes much stiffer (or softer) than the others [12].

On the other hand, analytical micromechanics models have much lower computational cost than FE or FFT-based methods. We will discuss several categories of analytical micromechanics methods. The first category of micromechanics methods begins from the work of Hashin and Shrikman [13, 14, 15], who gave the upper and lower bounds for the effective properties of heterogeneous materials based on variational principles. Their closed-form solutions depend on the volume fraction of the inclusion or secondary phase but ignore other key factors, such as the inclusion shapes and distributions. In order to improve the accuracy and universality of this model, higher-order bounds have been proposed which incorporate statistical microstructural information, such as two-point and three-point correlation functions [16, 17]. The second category of micromechanics methods dates back to the work of Eshelby [18], which gave the exact solution of the stress field for one ellipsoidal inclusion embedded in an infinite matrix. Several mean-field approaches were proposed based on Eshelby's solution, such as the Mori-Tanaka method [19] and self-consistent methods [20, 21, 22]. For polymer nanocomposite, these theories can be generalized for use with linear viscoelasticity by considering the Fourier transformation of the constitutive law to the frequency domain [23, 24]. Approaches based on Eshelby's solution are restricted to regular inclusion shapes such as ellipses in 2-Dimensions (2-D) and ellipsoids in 3-Dimensions (3-D). In order to deal with arbitrary inclusion shapes, Liu et al. developed self-consistent models which can consider arbitrary inclusion shape and strain distribution in the inclusion [25, 26].

A difficulty of most of the existing analytical micromechanics models is that simple shaped inclusions must remain unique, and the physical pictures behinds those models become vague once inclusions' ranges of influence begin to overlap and strong interactions begin to occur. Mori-Tanaka and self-consistent methods are sensitive to the volume fraction of the inclusion phase, but cannot distinguish between inclusions that are well dispersed (nonoverlaping), clustered (overlapping) or strongly interacted (overlapping). In order to account for the local interaction between a nanoparticle and the matrix material in polymer nanocomposites, interphase effects were incorporated by Diani et al. [27] who added an interphase layer around the filler using a four-phase model [22]. Although the volume fraction of the interphase layer can be calibrated to match the experimental data, its geometric information (e.g., its shape when multiple inclusions interact) is missing. Moreover, when inclusions interact with each other and the inclusion phase starts to dominate overall properties, assumptions of many micromechanics models may fail. For example, the Mori-Tanaka method [19] and its variants, which are specifically applied to polymer nanocomposites [23], assume that the representative inclusion (including the interphase region for polymer nanocomposites) is embedded in the matrix, which only captures the physics for a material with dilute/weakly interacting inclusions.

In this paper, we propose a new extended micromechanics method that naturally handles general overlapping inclusion geometries. The results of our new method is a model that addresses complex clusters of inclusions and the complex properties of interphase between several interacting inclusion, as discussed in Section 2. Mathematical formulations of overlapping conditions are introduced in Section 4. Section 5 shows the general scheme of the extended micromechanics, and its predictions using the Boolean-Poisson model are compared with DNS results. In Section 6, the extended micromechanics method for overlapping

geometries will be applied to predict interphase properties in a viscoelastic polymer composite based on experimental data. Concluding remarks are provided in Section 7.

## 2. Geometric Framework and Physics of Overlapping Inclusions

As a primer for our microstructural considerations, we first define inclusions and particles. For the remainder of this work, a particle is defined as a distinct phase where the chemical composition of the material differs from the matrix (e.g., a carbon-black filler in a polymer matrix is a particle). An inclusion is defined as any region where there material moduli are different from the matrix material (e.g., a carbon-black filler and its surrounding interphase region are together an inclusion). With this distinction, the term *inclusion overlap* describes a scenario where either particles *overlap* to form a cluster of particles or interphases overlap to form a region with unique interphase properties (see Figure 1). Thus, through the concept of overlapping inclusions we can treat dilute or weakly interacting systems, clustered particles, and interacting interphases all using one general geometric framework. Dilute systems occur when inclusions do not interact (such as in Eshelby's problem); whereas, in weakly interacting systems inclusions interact indirectly by affecting the mean matrix properties (such as in the Mori-Tanaka model). By allowing for overlapping interphases, the proposed model offers a succinct and general method to capture interphase properties regardless of the their spatially varying nature or the complexity of the inclusion network. By allowing for overlapping particles, the proposed model extends classical theories for simple particle shapes (such as the Eshelby and Mori-Tanaka methods) to any inclusion geometry that can be expressed as a union of simple shape.

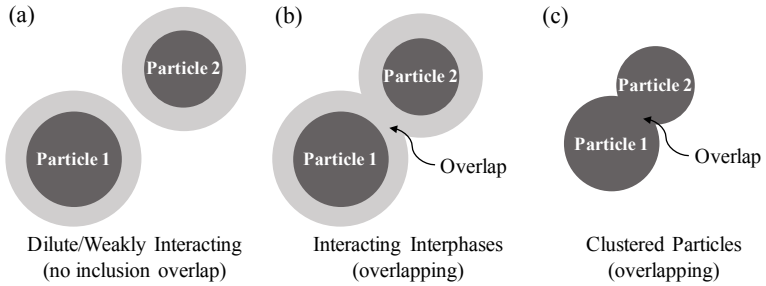


Figure 1: Three geometric inclusion configurations (a) dilute/weakly interacting inclusion, where inclusions do not overlap (b) interacting interphases, where interphases overlap but particles remain distinct (c) clustered particles, where the union of several simple particles forms arbitrarily complex clustered geometries.

This overlapping concept stems loosely from ideas of stochastic geometry which are often used to describe wireless networks [28] (e.g., cellular phone towers with overlapping ranges of transmission). For example, the Boolean-Poisson model employed in Section 5.2 is a common model in stochastic geometry.

As previously discussed, the interphase region around a particle is composed of matrix material but can have dramatically different material properties. When two or more particles are near enough to each other that their interphase regions overlap, the interphase properties in the overlapping region often takes on new material properties that differ both from the matrix and the previous (non-overlapping) interphase [4].

We will adopt two methods to account for these overlapping properties: additive and weighted-mean, where in the former, overlapping inclusion properties are summed and in the latter properties are computed via a weighted-mean (and the weighting determines the allowed amount of particle overlap). Formal definitions are given in equations (19) and (11). The utility of these overlapping methods is illustrated in Figure 2 and Figure 3.

Figure 2 shows the relative modulus in an overlapping region $\delta\mathbf{C}(\mathbf{x})$ normalized by the relative inclusion modulus $\delta\mathbf{C}^c$ for a system with constant modulus inclusions. For the weighted-mean case, Figure 2(a) shows large clusters with constant modulus, as would be expected in a polymer composite with irregular agglomerated fillers [29]. However, Figure 2(b) shows peaks in modulus, due to the additive overlap condition, which

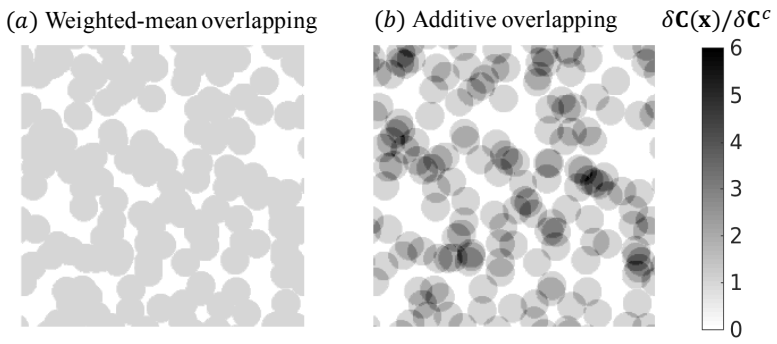


Figure 2: 2-D examples of Boolean-Poisson model under (a) weighted-mean (with all weights set to 1) and (b) additive overlapping conditions. The volume faction of the inclusion phase is 70%. The relative modulus after overlapping $\delta\mathbf{C}(\mathbf{x})$ is normalized by the inclusion modulus $\delta\mathbf{C}^c$.

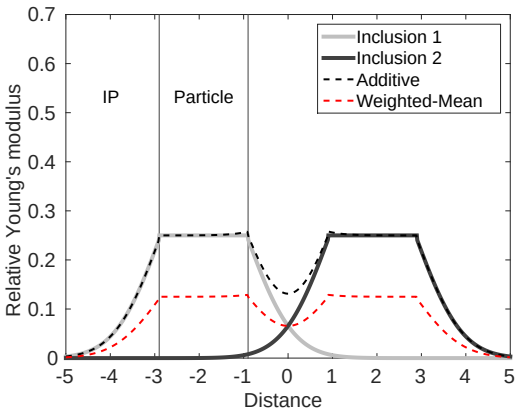


Figure 3: The example relative Young's modulus of two inclusions with an interphase (IP) region. The modulus of each particle is constant and the IP modulus is spatially varying. The weighted-mean profile is computed with equal particle and interphase weights.

does not seem physical. For this reason, the weighted mean method is preferred for clustered particles. However, an alternative scenario is shown in Figure 3 which illustrates the utility of the additive condition. As shown in the figure, when interphases with varying moduli overlap, the weighted-mean modulus does not capture the particle properties. Thus, the weighted-mean condition may predict a large, potentially unphysical drop in modulus. The additive modulus, however, captures the particle modulus well and results in interphase properties that vary smoothly between particles (as is suggested by the illustration in Figure 16 of [4]). While the weighted-mean modulus behaves well for constant interphase properties, the additive modulus is preferred for spatially varying interphase moduli.

## 3. Integral Equations and Homogenization of Multi-inclusion Systems

Let us first consider a heterogeneous material where all the phases are assumed to be linearly isotropic and elastic. The matrix material is denoted as phase 0. If there is no body force, the equilibrium condition in a material domain $\Omega$ can be written as

$$\frac{\partial[C_{ijkl}(\mathbf{x})\varepsilon_{kl}(\mathbf{x})]}{\partial x_i} = 0 \quad \text{in } \Omega, \tag{1}$$

where $\varepsilon_{kl}(\mathbf{x})$ is the local strain tensor. By treating the matrix material as a homogeneous reference medium and introducing the concept of polarization stress [30], the original equilibrium condition can be reformulated

as an integral equation in terms of the strain $\boldsymbol{\varepsilon}$,

$$\varepsilon_{ij}(\mathbf{x}) = \varepsilon^0_{ij} - \int_\Omega \Phi_{ijkl}(\mathbf{x},\mathbf{x}')\delta C_{klmn}(\mathbf{x}')\varepsilon_{mn}(\mathbf{x}')d\mathbf{x}' \quad \text{in } \Omega, \tag{2}$$

where $\varepsilon^0_{ij}$ is the far field strain in the homogeneous reference medium without the appearance of any heterogeneous phase, and where we let $\delta\mathbf{C}(\mathbf{x}) = \mathbf{C}(\mathbf{x}) - \mathbf{C}^0$. The fourth-order Green's function of the reference medium $\Phi_{ijkl}(\mathbf{x},\mathbf{x}')$ represents the strain contribution at $\mathbf{x}$ from a concentrated external stress at $\mathbf{x}'$. Expressions of Green's functions for isotropic 2-D plane strain and 3-D material can be found in [21]. The integral equation of strain is also known as Lippmann-Schwinger equation, and it should be noted that the reference medium does not have to share the same properties as the matrix material. However we choose it as the matrix material for the ease of developing the extended micromechanics method in Section 5.

By solving equation (2) in the material domain with prescribed boundary conditions, we can homogenize the local responses to get the macroscopic properties. Before proceeding to the details of homogenization, the material domain $\Omega$ is defined to be a RVE, so that its size greatly exceeds the wavelength of the local fluctuations of strain and stress fields. The overall properties of the RVE should not depend on the boundary conditions, and it can be treated as a homogeneous material at the macro-scale. According to the Hill-Mandel principle of macro-homogeneity [20], we have the following equation in the RVE domain $\Omega$,

$$\langle \boldsymbol{\sigma} : \boldsymbol{\varepsilon} \rangle_\Omega = \langle \boldsymbol{\sigma} \rangle_\Omega : \langle \boldsymbol{\varepsilon} \rangle_\Omega, \tag{3}$$

where ":" represents the tensor contraction, and $\langle ... \rangle_\Omega$ denotes the volume averaging operator inside $\Omega$. With the energy equivalence indicated by equation (3), the RVE can be treated as a homogeneous material so that an effective constitutive relationship can be defined as,

$$\langle \boldsymbol{\sigma} \rangle_\Omega = \bar{\mathbf{C}} : \langle \boldsymbol{\varepsilon} \rangle_\Omega, \tag{4}$$

where $\bar{\mathbf{C}}$ is the effective stiffness tensor of the heterogeneous material.

The average strain in the RVE can be determined by taking the volume average of strain inside $\Omega$,

$$\bar{\boldsymbol{\varepsilon}} = \langle \boldsymbol{\varepsilon} \rangle_\Omega = \frac{1}{|\Omega|}\int_\Omega \boldsymbol{\varepsilon}(\mathbf{x})d\mathbf{x}, \tag{5}$$

where $|\Omega|$ is the volume of the RVE. Furthermore, the average stress inside the RVE domain is

$$\bar{\boldsymbol{\sigma}} = \langle \boldsymbol{\sigma} \rangle_\Omega = \frac{1}{|\Omega|}\int_\Omega \left[\mathbf{C}^0 + \delta\mathbf{C}(\mathbf{x})\right]\boldsymbol{\varepsilon}(\mathbf{x}) = \mathbf{C}^0 : \bar{\boldsymbol{\varepsilon}} + \langle \delta\mathbf{C}(\mathbf{x}) : \boldsymbol{\varepsilon}(\mathbf{x}) \rangle_\Omega. \tag{6}$$

As we can see from equation (6), the key step in the homogenization is to calculate the *average polarization stress* $\langle \delta\mathbf{C}(\mathbf{x}) : \boldsymbol{\varepsilon}(\mathbf{x}) \rangle_\Omega$ as a function of a certain macroscopic quantity (e.g., average strain $\bar{\boldsymbol{\varepsilon}}$), and then the effective stiffness tensor can be computed based on equation (4). Due to inclusion overlapping, $\langle \delta\mathbf{C}(\mathbf{x}) : \boldsymbol{\varepsilon}(\mathbf{x}) \rangle_\Omega$ is not naturally a linear combination of the contribution from each individual inclusion, which blurs the physical picture behind most micromechanics methods which are based on a single representative inclusion. As will be shown in Section 4, this issue can be resolved by properly choosing the overlapping conditions, which govern the calculation of moduli in the overlapping region.

## 4. Mathematical Formulations of Overlapping

As discussed in Section 1, most existing micromechanics methods cannot account for overlapping inclusions. For example, let us consider a two-phase material with spherical inclusions embedded in the matrix. If the inclusions do not overlap, the matrix phase is always continuous and dominates the overall properties of the two-phase material. For no overlap (especially of an interphase region) to occur, the particle volume fraction must remain low, as particle spacing must stay relatively large to avoid interactions. However, when the inclusions can overlap, the inclusions can percolate through the matrix and become a competitor

of the matrix phase as the volume fraction increases. Most of the existing micromechanics methods (e.g., Mori-Tanaka method [19, 31] and self consistent method [20, 22]) can not account for these overlapping effects because they have no mechanism for dealing with the material properties in the overlapping regions. Another challenge in modeling the overlap is that the physics in the overlapping regions will vary with material system. Thus, many different overlapping conditions may be necessary to account for a wide range of overlapping phenomena.

In this section, we will introduce two basic overlapping conditions: 1) the weighted-mean overlapping condition and 2) the additive overlapping condition. Then the new strain definitions and modified integral equations in each inclusion, as well as expressions of the average polarization stress, will be derived under both conditions. A unified micromechanics method will be proposed in Section 5 to predict the effective properties of heterogeneous materials with overlapping effects.

Before introducing different overlapping conditions, we start with the RVE domain containing N overlapping inclusions. The domain of each inclusion is denoted as $\Omega^r$, with $r = 1, 2, ..., N$. Due to the existence of overlapping, we have

$$\bigcap_{r=1}^{N} \Omega^r \neq \emptyset. \tag{7}$$

The combined domain of all inclusion phases $\Omega^c$ and domain of the matrix phase $\Omega^m$ can be expressed as

$$\Omega^c = \bigcup_{r=1}^{N} \Omega^r, \quad \Omega^m = \Omega \setminus \bigcup_{r=1}^{N} \Omega^r. \tag{8}$$

Furthermore, the volume fraction of the inclusion phase is

$$f_c = \frac{|\Omega^c|}{|\Omega|}, \text{ with } |\Omega| = |\Omega^c| + |\Omega^m|. \tag{9}$$

Here we use the characteristic function to identify the region of each inclusion,

$$\chi_r(\mathbf{x}) = \begin{cases} 1 & \text{if } x \in \Omega^r \\ 0 & \text{otherwise} \end{cases}, \tag{10}$$

where $\chi^r(\mathbf{x})$ is the characteristic function of the $r$-th inclusion at point $\mathbf{x}$.

### *4.1. Weighted-mean overlapping condition*

First we will introduce the weighted-mean overlapping condition. The goal is to formulate the weighted-mean overlapping condition such that if the material is uniform in each inclusion before overlapping, the material properties are also uniform after overlapping (i.e., the resulting heterogeneous material only has two phases). We choose the relative stiffness tensor at any point in $\Omega^c$ to be

$$\delta\mathbf{C}(\mathbf{x}) = \frac{\sum_{r=1}^{N} \chi_r(\mathbf{x})\eta_r(\mathbf{x})\delta\mathbf{C}^r(\mathbf{x})}{\sum_{r=1}^{N} \chi_r(\mathbf{x})\eta_r(\mathbf{x})} = \frac{\sum_{r=1}^{N} \chi'_r(\mathbf{x})\delta\mathbf{C}^r(\mathbf{x})}{\sum_{r=1}^{N} \chi'_r(\mathbf{x})}, \tag{11}$$

where $\eta_r(\mathbf{x})$ is the weighting function in the $r$-th inclusion, and $\chi'_r(\mathbf{x})$ is the weighted characteristic function defined as

$$\chi'_r(\mathbf{x}) = \chi_r(\mathbf{x})\eta_r(\mathbf{x}). \tag{12}$$

The weighting function is employed–primarily–to enforce impenetrability of phases. The weighting function can be chosen to have a high value for phases that are considered to be impenetrable (i.e., no overlap allowed). For instance, a point in a high weighted particle region overlapped by a low weighted interphase region would take on the properties on the particle region, as if the overlap had not occurred (see Section

6). Substituting equation (11) into the original integral equation (2) and decompose the integral into each individual inclusion domain gives,

$$\varepsilon_{ij}(\mathbf{x}) = \varepsilon^0_{ij} - \sum_{s=1}^{N} \int_{\Omega_s} \Phi_{ijkl}(\mathbf{x}, \mathbf{x}') \left( \frac{\chi'_s(\mathbf{x}') \delta C^s_{klmn}(\mathbf{x}')}{\sum_{t=1}^{N} \chi'_t(\mathbf{x})} \right) \varepsilon_{mn}(\mathbf{x}') d\mathbf{x}' \quad \text{in } \Omega. \tag{13}$$

Decomposing the total strain at $\mathbf{x}'$ gives the strain in the $s$-th inclusion which can be defined as

$$\boldsymbol{\varepsilon}^s(\mathbf{x}') = \frac{\chi'_s(\mathbf{x}')}{\sum_{t=1}^{N} \chi'_t(\mathbf{x}')} \boldsymbol{\varepsilon}(\mathbf{x}'). \tag{14}$$

After substituting equation (14) into (13), we obtain

$$\varepsilon_{ij}(\mathbf{x}) = \sum_{s=1}^{N} \varepsilon^s_{ij}(\mathbf{x}) = \varepsilon^0_{ij} - \sum_{s=1}^{N} \int_{\Omega_s} \Phi_{ijkl}(\mathbf{x}, \mathbf{x}') \delta C^s_{klmn}(\mathbf{x}') \varepsilon^s_{mn}(\mathbf{x}') d\mathbf{x}' \quad \text{in } \Omega. \tag{15}$$

Also as imposed by the definition of the strain in each inclusion (see equation (14)), the following relationship must be satisfied,

$$\chi'_t(\mathbf{x}) \boldsymbol{\varepsilon}^s(\mathbf{x}) = \chi'_s(\mathbf{x}) \boldsymbol{\varepsilon}^t(\mathbf{x}) \quad \text{in } \Omega. \tag{16}$$

As a result, the integral equation in the $r$-th inclusion can be derived as

$$\left( \sum_{s=1}^{N} \chi'_s(\mathbf{x}) / \chi'_r(\mathbf{x}) \right) \varepsilon^r_{ij}(\mathbf{x}) = \varepsilon^0_{ij} - \sum_{s=1}^{N} \int_{\Omega_s} \Phi_{ijkl}(\mathbf{x}, \mathbf{x}') \delta C^s_{klmn}(\mathbf{x}') \varepsilon^s_{mn}(\mathbf{x}') d\mathbf{x}' \quad \text{in } \Omega^r. \tag{17}$$

As discussed in Section 3, the key term in the homogenization procedure is the average polarization stress $\langle \delta \mathbf{C}(\mathbf{x}) : \boldsymbol{\varepsilon}(\mathbf{x}) \rangle_\Omega$, and we can show that it can be computed as a summation of the contribution from each inclusion based on equation (11) and (14).

$$\langle \delta \mathbf{C}(\mathbf{x}) : \boldsymbol{\varepsilon}(\mathbf{x}) \rangle_\Omega = \frac{1}{|\Omega|} \int_\Omega \delta \mathbf{C}(\mathbf{x}) : \boldsymbol{\varepsilon}(\mathbf{x}) d\mathbf{x} = \frac{1}{|\Omega|} \sum_{s=1}^{N} \int_{\Omega_s} \delta \mathbf{C}^s(\mathbf{x}) \boldsymbol{\varepsilon}^s(\mathbf{x}) d\mathbf{x}. \tag{18}$$

### *4.2. Additive overlapping condition*

Another way of overlapping inclusions is to take the summation of relative stiffness tensors of all the inclusions involved in the overlapping. By using the characteristic function defined in equation (10), the relative stiffness tensor at any point in $\Omega$ can be written as

$$\delta \mathbf{C}(\mathbf{x}) = \sum_{r=1}^{N} \chi_r(\mathbf{x}) \delta \mathbf{C}^r(\mathbf{x}). \tag{19}$$

Similarly, we can substitute equation (19) into the original integral equation (2) and decompose the integral into each individual inclusion domain, so that the new integral equation in $\Omega$ becomes

$$\varepsilon_{ij}(\mathbf{x}) = \varepsilon^0_{ij} - \sum_{s=1}^{N} \int_{\Omega_s} \Phi_{ijkl}(\mathbf{x}, \mathbf{x}') \chi_s(\mathbf{x}') \delta C^s_{klmn}(\mathbf{x}') \varepsilon_{mn}(\mathbf{x}') d\mathbf{x}' \quad \text{in } \Omega. \tag{20}$$

In equation (20), the strain in the $s$-th inclusion can be defined as

$$\boldsymbol{\varepsilon}^s(\mathbf{x}') = \chi_s(\mathbf{x}') \boldsymbol{\varepsilon}(\mathbf{x}'). \tag{21}$$

According to the definition of $\boldsymbol{\varepsilon}^s(\mathbf{x}')$, the following condition should be satisfied,

$$\chi_t(\mathbf{x})\boldsymbol{\varepsilon}^s(\mathbf{x}) = \chi_s(\mathbf{x})\boldsymbol{\varepsilon}^t(\mathbf{x}) \quad \text{in } \Omega. \tag{22}$$

Finally, the integral equation in the $r$-th inclusion becomes

$$\varepsilon^r_{ij}(\mathbf{x}) = \varepsilon^0_{ij} - \sum_{s=1}^{N} \int_{\Omega_s} \Phi_{ijkl}(\mathbf{x},\mathbf{x}')\delta C^s_{klmn}(\mathbf{x}')\varepsilon^s_{mn}(\mathbf{x}')d\mathbf{x}' \quad \text{in } \Omega^r. \tag{23}$$

It can be shown that equation (18) for the average polarization stress $\langle\delta\mathbf{C}(\mathbf{x}) : \boldsymbol{\varepsilon}(\mathbf{x})\rangle_\Omega$ is also satisfied under additive overlapping condition.

In Table 1, we summarize the mathematical formulations of both weighted-mean and additive overlapping conditions.

Table 1: Summary of mathematical formulations for weighted-mean and additive overlapping conditions.

| | Weighted-mean overlapping | Additive overlapping |
|---|---|---|
| Overall relative stiffness tensor | $\delta\mathbf{C}(\mathbf{x}) = \dfrac{\sum_{r=1}^{N}\chi'_r(\mathbf{x})\delta\mathbf{C}^r(\mathbf{x})}{\sum_{r=1}^{N}\chi'_r(\mathbf{x})}$ | $\delta\mathbf{C}(\mathbf{x}) = \sum_{r=1}^{N}\chi_r(\mathbf{x})\delta\mathbf{C}^r(\mathbf{x})$ |
| Definition of strain in each inclusion | $\boldsymbol{\varepsilon}^s(\mathbf{x}') = \dfrac{\chi'_s(\mathbf{x}')}{\sum_{t=1}^{N}\chi'_t(\mathbf{x}')}\boldsymbol{\varepsilon}(\mathbf{x}')$ | $\boldsymbol{\varepsilon}^s(\mathbf{x}') = \chi_s(\mathbf{x}')\boldsymbol{\varepsilon}(\mathbf{x}')$ |
| The integral equation in each inclusion | $L^r(\mathbf{x})\varepsilon^r_{ij}(\mathbf{x}) = \varepsilon^0_{ij} - \sum_{s=1}^{N}\int_{\Omega_s}\Phi_{ijkl}(\mathbf{x},\mathbf{x}')\delta C^s_{klmn}(\mathbf{x}')\varepsilon^s_{mn}(\mathbf{x}')d\mathbf{x}'$ | |
| | $L^r(\mathbf{x}) = \sum_{s=1}^{N}\chi'_s(\mathbf{x})/\chi'_r(\mathbf{x})$ | $L^r(\mathbf{x}) = 1$ |
| Average polarization stress | $\langle\delta\mathbf{C}(\mathbf{x}) : \boldsymbol{\varepsilon}(\mathbf{x})\rangle_\Omega = \dfrac{1}{\lvert\Omega\rvert}\sum_{s=1}^{N}\int_{\Omega_s}\delta\mathbf{C}^s(\mathbf{x})\boldsymbol{\varepsilon}^s(\mathbf{x})d\mathbf{x}$ | |

By comparing equation (23) with (17), as well as in Table 1, we can see that the only difference is the coefficient $L^r(\mathbf{x})$ before $\varepsilon^r_{ij}(\mathbf{x})$ on the left hand side, due to different definitions of the strain in each inclusion. It should be noted, that the entire procedure of deriving the integral equation in each inclusion–based on the given overlapping condition–is general, and it can be applied to other overlapping conditions as long as the overall relative stiffness tensor is a linear combination of those in each inclusion. Although the overlap condition could take many forms based on the physics of a material system, we will focus on the weighted-mean and additive overlapping conditions in this paper.

## 5. Extended Micromechanics Method for Overlapping Geometries

### *5.1. General homogenizing scheme*

In this section, we aim to calculate the effective constitutive equation for a heterogeneous material containing multiple overlapping inclusions. Rather than using full direct numerical simulation, which is time-consuming (especially for complex microstructures with important features on scales much smaller than the RVE, such as nanocomposite), we will develop an analytical micromechanics method to homogenize the multi-inclusion system more efficiently, and to take into account inclusion overlap.

The first step is to elucidate the essential assumption of the extended micromechanics methods for overlapping geometries. In order to probe the properties at a given point, we will insert a new *test* inclusion

randomly into the original material. Since overlapping is allowed, this *test* inclusion may overlap with the matrix material and other existing inclusions at the same time. In order to simplify the physical picture, the dimension of the *test* inclusion is assumed to be orders of magnitude smaller than the original inclusions, while its shape and material constituents are kept the same. Therefore, the strain and material properties surrounding the *test* inclusion can be considered constant, and the overlapping state in the *test* inclusion can be considered homogeneous. For example, if the *test* inclusion was relatively large, it could overlap with one inclusion through part of its domain and two inclusions through another part, and the physical picture would be more complicated. Under this assumption, the *test* inclusion is equivalent to a sampling point in the original material, and the outcomes of this random testing process form a sample space $\Xi$,

$$\Xi = \{\xi_0, \xi_1, \xi_2, ...\}, \quad \text{with} \sum_{\xi_i \in \Xi} p(\xi_i) = 1, \tag{24}$$

where $\xi_i$ is an overlapping state in $\Xi$ at the sampling point (or *test* inclusion), and $p$ is a probability function mapping $\Xi$ to $[0, 1]$. For examples, $p(\xi_0)$ represents the probability that the sampling point is in the matrix material, and $p(\xi_3)$ in Boolean-Poisson model (see equation (37)) represents the probability that the sampling point overlaps with three inclusions.

For the overlapping state $\xi_0$, there is no overlapping of inclusions at the sampling point, so that the *test* inclusion is inserted into the matrix material as shown in Figure 5(a). For this state, the strain in the *test* inclusion $\boldsymbol{\varepsilon}^{\text{test}}$ can be related to the average strain in the matrix $\bar{\boldsymbol{\varepsilon}}^m$ (similar to the concept in the Mori-Tanaka method [19, 31]),

$$\boldsymbol{\varepsilon}^{\text{test}}_{(\xi_0)} = \mathbf{T}_{(\xi_0)} : \bar{\boldsymbol{\varepsilon}}^m, \tag{25}$$

where $\mathbf{T}_{(\xi_0)}$ depends on the shape of the inclusion, the properties of both the inclusion and matrix materials, and is not necessarily uniform in the inclusion. However, when the test inclusion is ellipsoidal in 3D (or elliptic in 2-D) with uniform material properties, $\mathbf{T}_{(\xi_0)}$ will be a constant relating to the Eshelby's tensor $\mathbf{S}^m$ of the matrix material (more details are provided in Section 5.2). More interestingly, Benveniste has shown that equation (25) takes inclusion interactions into account although $\boldsymbol{\varepsilon}^{\text{test}}_{(\xi_0)}$ is only a function of $\bar{\boldsymbol{\varepsilon}}^m$ [31].

For the overlapping state $\xi_i (i \neq 0)$, the *test* inclusion is inserted into a non-matrix region with a stiffness tensor $\mathbf{C}_{(\xi_i)}$ and strain $\hat{\boldsymbol{\epsilon}}_{(\xi_i)}$. Similarly, the strain in the test inclusion can be determined by

$$\boldsymbol{\varepsilon}^{\text{test}}_{(\xi_i)} = \mathbf{T}_{(\xi_i)} : \hat{\boldsymbol{\epsilon}}_{(\xi_i)} \quad \text{for } i \neq 0. \tag{26}$$

Other than the inclusion shape and material properties, $\mathbf{T}_{(\xi_i)}$ is also related to the overlapping condition and the corresponding integral equation (17) or (23).

In order to approximate the strain $\hat{\boldsymbol{\epsilon}}_{(\xi_i)}$ we use the strain concentration tensor $\mathbf{A}$ as

$$\hat{\boldsymbol{\epsilon}}_{(\xi_i)} = \mathbf{A}_{(\xi_i)} : \bar{\boldsymbol{\varepsilon}}. \tag{27}$$

where $\mathbf{A}_{(\xi_i)}$ is the strain concentration tensor of the overlapping state $\xi_i$. Inserting equation (27) in equation (26) gives:

$$\boldsymbol{\varepsilon}^{\text{test}}_{(\xi_i)} = \left(\mathbf{T}_{(\xi_i)} : \mathbf{A}_{(\xi_i)}\right) : \bar{\boldsymbol{\varepsilon}} \quad \text{for } i \neq 0, \tag{28}$$

For a 3-D spherical (or circular in 2-D) inclusion embedded in a homogeneous medium, the strain concentration tensor becomes a function of Eshelby's tensor, the properties of the inclusion, and the properties of the surrounding medium. Here we will assume the inclusion has a stiffness tensor $\mathbf{C}_{(\xi_i)}$. The surrounding material properties are assumed to be that of the effective medium $\bar{\mathbf{C}}$, as in self-consistent methods [20, 22, 24]. The strain concentration tensor of overlapping state $\xi_i$ then becomes:

$$\mathbf{A}_{(\xi_i)} = \left[\mathbf{I} + \bar{\mathbf{S}} : \bar{\mathbf{C}}^{-1} : (\mathbf{C}_{(\xi_i)} - \bar{\mathbf{C}})\right]^{-1} \quad \text{for } i \neq 0, \tag{29}$$

where $\mathbf{I}$ is the forth-order identity tensor and by $\bar{\mathbf{S}}$ denotes the Eshelby's tensor of the effective medium. Using equation (29) the strain in the *test* inclusion becomes:

$$\boldsymbol{\varepsilon}^{\text{test}}_{(\xi_i)} = \left(\mathbf{T}_{(\xi_i)} : \left[\mathbf{I} + \bar{\mathbf{S}} : \bar{\mathbf{C}}^{-1} : (\mathbf{C}_{(\xi_i)} - \bar{\mathbf{C}})\right]^{-1}\right) : \bar{\boldsymbol{\varepsilon}} \quad \text{for } i \neq 0, \tag{30}$$

An illustration of the simplified model for state $\xi_i (i \neq 0)$ is provided in Figure 4(b).

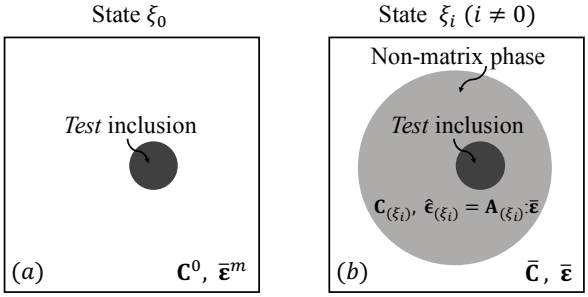


Figure 4: Illustration of the physical models for different overlapping states: (a) In state $\xi_0$, the *test* inclusion is embedded into the matrix material with stiffness tensor $\mathbf{C}^0$ and strain $\bar{\boldsymbol{\varepsilon}}^m$; (b) In state $\xi_i (i \neq 0)$, the *test* inclusion in embedded into a non-matrix region with stiffness tensor $\mathbf{C}_{(\xi_i)}$ and strain $\boldsymbol{\epsilon}_{(\xi_i)}$, which is related to the overall average strain $\bar{\boldsymbol{\varepsilon}}$ through the concentration factor $\mathbf{A}_{(\xi_i)}$ defined in equation (29).

From equation (25) and (28), the expected value of strain in the *test* inclusion $\langle \boldsymbol{\epsilon}^{\text{test}} \rangle$ is defined as

$$\langle \boldsymbol{\epsilon}^{\text{test}} \rangle = \sum_{\xi_i \in \Xi} p(\xi_i) \boldsymbol{\epsilon}^{\text{test}}_{(\xi_i)} = p(\xi_0) \mathbf{T}_{(\xi_0)} : \bar{\boldsymbol{\varepsilon}}^m + \left[ \sum_{\xi_i \in (\Xi \setminus \xi_0)} p(\xi_i) \mathbf{T}_{(\xi_i)} : \mathbf{A}_{(\xi_i)} \right] : \bar{\boldsymbol{\varepsilon}} \tag{31}$$

In addition, the following equation for the average strain must be satisfied,

$$\bar{\boldsymbol{\varepsilon}} = (1 - f_c) \bar{\boldsymbol{\varepsilon}}^m + f_c \bar{\boldsymbol{\varepsilon}}^c, \tag{32}$$

where $\bar{\boldsymbol{\varepsilon}}^c$ is the average strain in the overall inclusion phase. By assuming that all of the inclusions share the same expectation of strain with the *test* inclusion, $\bar{\boldsymbol{\varepsilon}}^c$ can be written as a function of $\langle \boldsymbol{\epsilon}^{\text{test}} \rangle$,

$$\bar{\boldsymbol{\varepsilon}}^c = \mathbf{F}(\langle \boldsymbol{\epsilon}^{\text{test}} \rangle), \tag{33}$$

where $\mathbf{F}$ is a function depending on the overlapping condition (as shown in equation (46) and (54)). For a material with non-overlapping inclusions, we simply have $\bar{\boldsymbol{\varepsilon}}^c = \langle \boldsymbol{\epsilon}^{\text{test}} \rangle$.

Finally, based on equation (3), (6) and (18), the effective stiffness $\bar{\mathbf{C}}$ can be calculated. As we can see from equation (31), the extended micromechanics method is self-consistent since $\mathbf{A}_{(\xi_i)}$ depends on $\bar{\mathbf{C}}$; therefore, the effective stiffness tensor will be calculated iteratively using a fix-point method in this paper. A special case exists when the inclusions do not overlap with each other (or $p(\xi_0) = 1$), and equation (31) becomes

$$\langle \boldsymbol{\epsilon}^{\text{test}} \rangle = \mathbf{T}_{(\xi_0)} : \bar{\boldsymbol{\varepsilon}}^m \quad \text{if } p(\xi_0) = 1. \tag{34}$$

In this case, the extended micromechanics method reproduces the Mori-Tanaka method, and no iteration is required when solving the effective stiffness tensor.

### *5.2. Basics of Boolean-Poisson model*

In stochastic geometry, the Boolean-Poisson model (or Boolean model) is a simple and commonly used method to generate overlapping geometries [32]. In this paper, all the $N$ inclusions are identical and chosen to be spherical in 3-D (or circular in 2-D) with same radius $R^c$ and volume $V^c$. The center of each inclusion is randomly and independently inserted into the RVE domain $\Omega$ obeying a uniform distribution, and the resulting union of the overlapping inclusion is a realization of the Boolean-Poisson model. The procedure also refers to a stationary Poisson point process in $\Omega$ with a rate $\lambda$, which is defined as

$$\lambda = N / |\Omega|. \tag{35}$$

The number of inclusion centers $K$ at any point in $\Omega$ is a Poisson random variable whose probability function is

$$p(K=k)=\frac{\lambda^k}{k!}e^{-\lambda}, \tag{36}$$

where $k!$ denotes the $k$ factorial. The expected value of $K$ is equal to the rate $\lambda$.

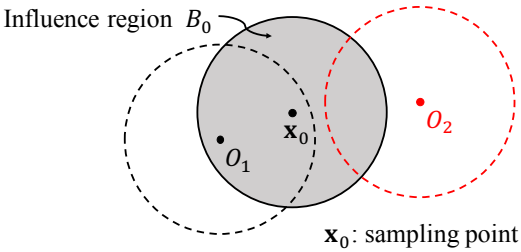


Figure 5: Illustration of the influence region $B_0$ centering at the sampling point $\mathbf{x}_0$. The center of the first inclusion $O_1$ is inside $B_0$, so that it overlaps with $\mathbf{x}_0$. While for the second inclusion, its center $O_2$ is outside $B_0$ so that it will not influence the material properties at $\mathbf{x}_0$.

Due to the simplicity of Boolean-Poisson model, we can define $\xi_i$ as the state where there are $i$ inclusions overlapping at a sampling point $\mathbf{x}_0$,

$$\sum_{r=1}^{N}\chi_r(\mathbf{x}_0)=i \quad \text{at state } \xi_i. \tag{37}$$

In order to calculate the probability function of $\xi_i$, we will first draw a sphere with radius $R^c$ centering at $\mathbf{x}_0$, called the influence region $B_0$. As we can see from Figure 5, if the center of any inclusion is inserted into the influence region, the inclusion will contribute to the overlapping at $\mathbf{x}_0$. Since the random processes at different points in Boolean-Poisson model are independent from each other, the total number of inclusion whose centers are in the influence region $B_0$ also follows a Poisson distribution with a rate $\lambda V^c$. Finally, we obtain the probability function of the overlapping states:

$$p(\xi_i)=\frac{(\lambda V^c)^i}{i!}e^{-\lambda V^c}. \tag{38}$$

Another important quantity in the Boolean-Poisson model is the volume fraction of the inclusion phase $f_c$, defined in equation (9). A phase density function $\rho(\mathbf{x})\in[0,1]$ is introduced for the analysis. The value of $\rho(\mathbf{x})$ is equal to 0 if $\mathbf{x}$ is in the matrix phase, or 1 if $\mathbf{x}$ is in the inclusion phase. Since the phase density function needs be kept at 1 in the inclusion phase after overlapping (analogous to weighted-mean overlapping condition for the relative stiffness tensor), the phase density function in the $r$-the inclusion $\rho^r(x)$ can be determined by

$$\left(\sum_{s=1}^{N}\chi_s(\mathbf{x})\right)\rho^r(\mathbf{x})=1 \quad \text{in } \Omega^r. \tag{39}$$

As in the general scheme discussed in Section 5.1, a *test* inclusion is inserted at the sampling point $\mathbf{x}_0$ in the Boolean-Poisson model. Based on equation (37), the expected value of the phase density function $\langle\rho^c\rangle$ in the *test* inclusion can be derived as

$$\langle\rho^c\rangle=\sum_{\xi_i\in\Xi}p(\xi_i)\rho^c_{(\xi_i)}=\sum_{i=0}^{\infty}\frac{1}{i+1}p(\xi_i)=(\lambda V^c)^{-1}(1-e^{-\lambda V^c}) \tag{40}$$

Then the volume fractions of the inclusion phase and matrix phase are

$$f_c=\frac{N}{|\Omega|}\langle\rho^c\rangle V^c=1-e^{-\lambda V^c} \quad \text{and } f_m=1-f_c=e^{-\lambda V^c}. \tag{41}$$

These values are consistent with the theoretical volume fractions obtained through other methods for Boolean-Poisson's model [32], which indicates that our scheme of introducing a *test* inclusion is capable of capturing essential features of overlapping.

### *5.3. Results for Boolean-Poisson model under different overlapping conditions*

In this section, we will use the extended micromechanics method to predict the effective stiffness tensors of the Boolean-Poisson model under weighted-mean and additive overlapping conditions; illustrations of these results in 2-D are shown in Figure 2. The predictions will be compared with DNS results computed by the FFT-based method introduced by Moulinec and Suquet [11]. The original stiffness tensor before overlapping is uniform and equal to $\mathbf{C}^c$ in each inclusion.

We will consider the homogenization of the Boolean-Poisson model in the cases of spherical voids or spherical hard inclusions in 3-D. All the material interfaces are assumed to be perfectly bonded. The Young's modulus and Poisson's ratio of the matrix material are $E^0 = 1$ GPa and $\nu^0 = 0.3$. The material properties of hard inclusions are $E^c = 100$ GPa and $\nu^c = 0.3$. Due to convergence issues with the FFT-based DNS methods for infinite contrasted material properties [11, 12], the Young's modulus of "void" is chosen to be a small value (0.001 GPa) rather than equal to 0 GPa. In the FFT-based computations, we ran 6 samples on $200^3$ grids for each set of material parameters.

*1) Weighted-mean overlapping condition*

For the weighted-mean overlapping condition, the weighting function of each inclusion $\eta_r(\mathbf{x})$ is chosen to be equal to 1, so that $\chi'_r(\mathbf{x}) = \chi_r(\mathbf{x})$. In the non-matrix region (i.e., overlapping state $\xi_i (i \neq 0)$), we have

$$\mathbf{C}_{(\xi_i)} = \mathbf{C}^c \quad \text{and } \mathbf{A}_{(\xi_i)} = \left[\mathbf{I} + \bar{\mathbf{S}} : \bar{\mathbf{C}}^{-1} : (\mathbf{C}^c - \bar{\mathbf{C}})\right]^{-1} \quad \text{for } i \neq 0. \tag{42}$$

Based on the inclusion-wise integral equation (17) under weighted-mean overlapping condition and Eshelby's solution for spherical inclusions, the concentration factors can be determined as,

$$\mathbf{T}_{(\xi_0)} = \left[\mathbf{I} + \mathbf{S}^0 : (\mathbf{C}^0)^{-1} : (\mathbf{C}^c - \mathbf{C}^0)\right]^{-1} \tag{43}$$

and

$$\mathbf{T}_{(\xi_i)} = \frac{1}{i+1}\left[\mathbf{I} + \mathbf{S}_{(\xi_i)} : \mathbf{C}^{-1}_{(\xi_i)} : (\mathbf{C}^c - \mathbf{C}_{(\xi_i)})\right]^{-1} = \frac{1}{i+1} \quad \text{for } i \neq 0, \tag{44}$$

Where the $1/(i+1)$ term comes from the coefficient before $\varepsilon^r_{ij}(\mathbf{x})$ in equation (17) (or $L^r(\mathbf{x})$ in Table 1). Also in equation (44), $\mathbf{C}_{(\xi_i)} = \mathbf{C}^c$ in accordance with equation (42), resulting in the cancellation of the stiffness terms. By substituting equation (38) and (44) into (31), the expectation of strain in the *test* inclusion under weighted-mean overlapping condition becomes

$$\langle \boldsymbol{\varepsilon}^{\text{test}} \rangle = e^{-\lambda V^c} \mathbf{T}_{(\xi_0)} : \bar{\boldsymbol{\varepsilon}}^m + (\rho^c - e^{-\lambda V^c}) \mathbf{A}_{(\xi_i)} : \bar{\boldsymbol{\varepsilon}}. \tag{45}$$

Then based on the definition of inclusion-wise strain in equation (14), it can be shown that the average strain in the inclusion phase is

$$\bar{\boldsymbol{\varepsilon}}^c = \frac{\lambda V^c}{f_c} \langle \boldsymbol{\varepsilon}^{\text{test}} \rangle, \tag{46}$$

and equation (32) for the overall average strain becomes

$$\bar{\boldsymbol{\varepsilon}} = (1 - f_c)\bar{\boldsymbol{\varepsilon}}^m + \lambda V^c \langle \boldsymbol{\varepsilon}^{\text{test}} \rangle, \tag{47}$$

with the volume faction of inclusion phase $f_c$ provided in equation (41). Moreover, the overall average stress defined in equation (6) can be written as

$$\bar{\boldsymbol{\sigma}} = \mathbf{C}^0 : \bar{\boldsymbol{\varepsilon}} + \lambda V^c (\mathbf{C}^c - \mathbf{C}^0) : \langle \boldsymbol{\varepsilon}^{\text{test}} \rangle. \tag{48}$$

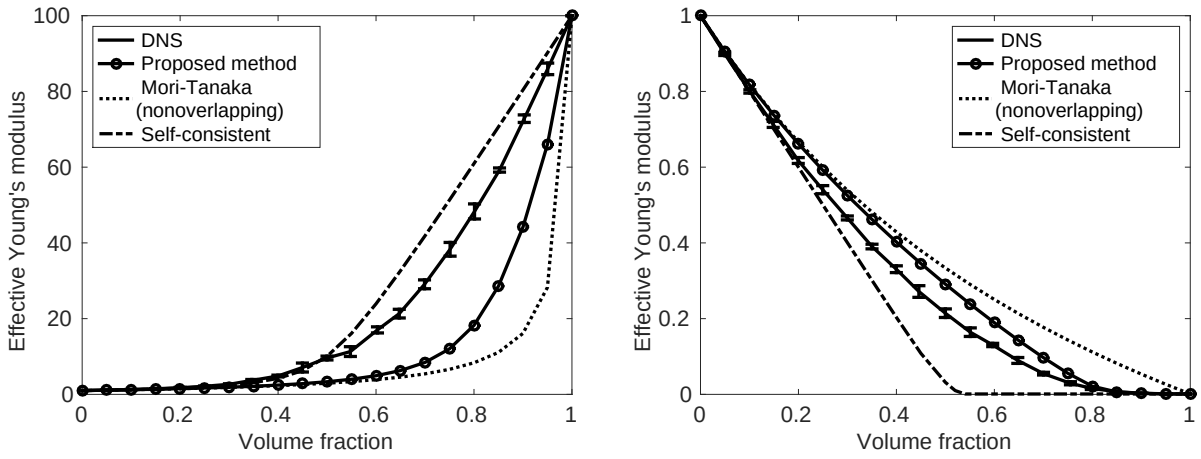


Figure 6: Effective Young's modulus of Boolean-Poisson model under additive overlapping condition with hard inclusions (left) and "voids"(right) vs. volume fraction of the inclusion phase. Each DNS data point has 6 samples on a $200^3$ grid.

Combining equation (45), (47) and (48), $\bar{\boldsymbol{\sigma}}$ can be eventually expressed as $\bar{\boldsymbol{\sigma}} = \bar{\mathbf{C}} : \bar{\boldsymbol{\varepsilon}}$. The effective stiffness tensor $\bar{\mathbf{C}}$ of the Boolean-Poisson model under weighted-mean overlapping condition is given by

$$\bar{\mathbf{C}} = \mathbf{C}^0 + \lambda V^c (\mathbf{C}^c - \mathbf{C}^0) : \frac{\mathbf{T}_{(\xi_0)} + (\rho^c - e^{-\lambda V^c})\mathbf{A}_{(\xi_i)}}{\mathbf{I} + \lambda V^c \mathbf{T}_{(\xi_0)}} \tag{49}$$

with $\mathbf{T}_{(\xi_0)}$ and $\mathbf{A}_{(\xi_i)}$ defined in equation (43) and (42)

Results of Boolean-Poisson model for hard inclusions and "voids" (soft inclusions) under weighted-mean overlapping condition are shown in Figure 6. In both situations, the effective Young's modulus vs. inclusion volume fraction curves predicted by the proposed method are bound by the Mori-Tanaka method and Hill's self-consistent method. Comparing to the DNS results, the proposed method underestimates the effective Young's modulus for hard inclusions, and overestimate it for voids. In particular, the predicted modulus becomes negligible for a critical void volume fraction of $f_c \approx 0.85$ which agrees with the DNS result very well, while the self-consistent method estimates this critical volume fraction to be $f_c = 0.50$.

More importantly, the proposed method can account for the overlapping effects while the Mori-Tanaka and self-consistent methods only account for volume fraction of the inclusions phase. For example the proposed model can account for the distribution of inclusions through the Boolean-Poisson model or a non-overlapping model; whereas, the Mori-Tanaka and self-consistent method cannot account for inclusion distributions.

*2) Additive overlapping condition*

For the additive overlapping condition, the material in the inclusion phase is heterogeneous and the overall stiffness tensor is proportional to the number of inclusions involved in the overlapping. For overlapping state $\xi_i (i \neq 0)$, the overlapping stiffness tensor and the corresponding strain concentration tensor are

$$\mathbf{C}_{(\xi_i)} = i(\mathbf{C}^c - \mathbf{C}^0) + \mathbf{C}^0 \quad \text{and} \quad \mathbf{A}_{(\xi_i)} = \{\mathbf{I} + \bar{\mathbf{S}} : \bar{\mathbf{C}}^{-1} : \left[i(\mathbf{C}^c - \mathbf{C}^0) + \mathbf{C}^0 - \bar{\mathbf{C}}\right]\}^{-1} \quad \text{for } i \neq 0. \tag{50}$$

As we can see from equation (50), $\mathbf{C}_{(\xi_i)}$ and $\mathbf{A}_{(\xi_i)}$ now varies with the overlapping state $\xi_i$. Based on the inclusion-wise integral equation (23) under additive overlapping condition and Eshelby's solution for spherical inclusions, the concentration factors for different overlapping states can be determined as

$$\mathbf{T}_{(\xi_0)} = \left[\mathbf{I} + \mathbf{S}^0 : (\mathbf{C}^0)^{-1} : (\mathbf{C}^c - \mathbf{C}^0)\right]^{-1} \tag{51}$$

and

$$\mathbf{T}_{(\xi_i)} = \left[\mathbf{I} + \mathbf{S}_{(\xi_i)} : \mathbf{C}^{-1}_{(\xi_i)} : (\mathbf{C}^c - \mathbf{C}^0)\right]^{-1} \quad \text{for } i \neq 0, \tag{52}$$

where, $\mathbf{T}_{(\xi_i)}$ depends on the overlapping state. Substituting equation (38) into (31) gives the expectation

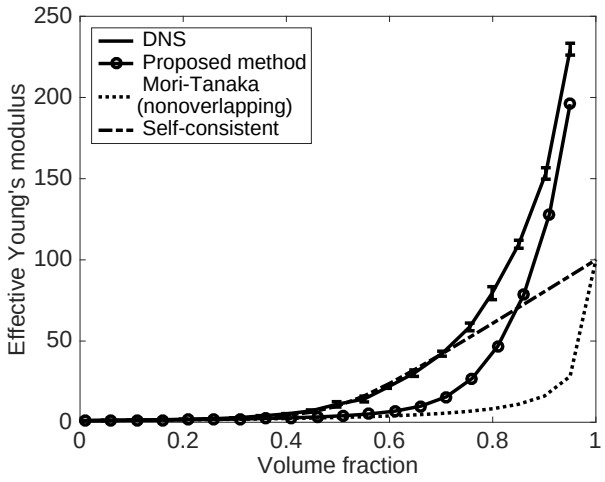


Figure 7: Effective Young's modulus of Boolean-Poisson model under additive overlapping condition as a function of the volume fraction of the inclusion phase. Each DNS data point has 6 samples on a $200^3$ grid.

of strain in the *test* inclusion under additive overlapping condition

$$\langle \boldsymbol{\varepsilon}^{\text{test}} \rangle = e^{-\lambda V^c} \left\{ \mathbf{T}_{(\xi_0)} : \bar{\boldsymbol{\varepsilon}}^m + \left[ \sum_{i=1}^{\infty} \frac{(\lambda V^c)^i}{i!} \mathbf{T}_{(\xi_i)} : \mathbf{A}_{(\xi_i)} \right] : \bar{\boldsymbol{\varepsilon}} \right\}. \tag{53}$$

Similarly, the average strain in the inclusion phase $\bar{\boldsymbol{\varepsilon}}^c$ can be related to $\langle \boldsymbol{\varepsilon}^{\text{test}} \rangle$ through equation (21),

$$\bar{\boldsymbol{\varepsilon}}^c = \langle \boldsymbol{\varepsilon}^{\text{test}} \rangle \tag{54}$$

Then the overall average strain can be expressed as

$$\bar{\boldsymbol{\varepsilon}} = (1 - f_c)\bar{\boldsymbol{\varepsilon}}^m + f_c \boldsymbol{\varepsilon}^c, \tag{55}$$

However, the expression of the average stress stays the same as equation (48),

$$\bar{\boldsymbol{\sigma}} = \mathbf{C}^0 : \bar{\boldsymbol{\varepsilon}} + \lambda V^c (\mathbf{C}^c - \mathbf{C}^0) : \boldsymbol{\varepsilon}^c. \tag{56}$$

With equation (53), (55) and (56), the effective stiffness tensor $\bar{\mathbf{C}}$ of Boolean-Poisson model under additive overlapping condition can be calculated as

$$\bar{\mathbf{C}} = \mathbf{C}^0 + \lambda V^c (\mathbf{C}^c - \mathbf{C}^0) : \frac{\mathbf{T}_{(\xi_0)} + e^{-\lambda V^c} \sum_{i=1}^{\infty} \frac{(\lambda V^c)^i}{i!} \mathbf{T}_{(\xi_i)} : \mathbf{A}_{(\xi_i)}}{\mathbf{I} + f_c \mathbf{T}_{(\xi_0)}}, \tag{57}$$

where $\mathbf{T}_{(\xi_0)}$ and $\mathbf{A}_{(\xi_i)}$ are defined in equation (51) and (50). In equation (57), the summation on the right hand side should be truncated for numerical calculation since no simplified analytical form exists. In the following 3-D example, $\lambda V^c$ will go up to 5 ($f_c = 0.993$), so we will keep 25 terms in the summation to guarantee that the coefficients $(\lambda V^c)^i / i!$ of the abandoned terms are less than $1 \times 10^{-8}$.

Results of Boolean-Poisson model for hard inclusions under the additive overlapping condition are shown in Figure 7. The proposed method captures the DNS trend well, especially at high volume fractions. Both the Mori-Tanaka and the self-consistent method cannot consider the additive overlapping effect, so they do not perform well at high volume fraction of the inclusion phase. However, if we switch from the original Boolean-Poisson model to a non-overlapping model, our proposed method will degrade to the Mori-Tanaka method.

### *5.4. Extension to other models*

We have derived the analytical form of the extended micromechanics method for the Boolean-Poisson model under weighted-mean and additive overlapping conditions. The method can be applied to more complex conditions which may account for material composition and shape of each inclusion, as well as the spatial distribution of the inclusions. Examples of these general conditions are listed as follow:

(i) The material properties do not have to be uniform within each inclusion. In Section 6 for polymer nanocomposites, the inclusion consists of a nano-particle surrounded by a polymer shell (interphase). Since each inclusion has two material phases in this case, the overlapping states in the sample space $\Xi$ will be more diverse. On the other hand, Eshelby's solution may not be applicable to multiphase inclusion and the strain becomes nonuniform in the inclusion. Other than introducing appropriate assumptions to recover the Eshelby's solution as in Section 6.1, another possible solution is to discretize the inclusion based on the volume-integral method. More details can be found in [25].

(ii) We can also put more restrictions on how inclusions are inserted into the matrix material. An extreme case is when overlapping inclusions are not allowed, and the extended micromechanics will reproduce the Mori-Tanaka method as mentioned in Section 5.1. Another good example is the penetrable-concentric-shell or "cherry-pit" model [17, 33], where the inclusions are only partially inter-penetrable. In cherry-pit model, the spacial distribution of each inclusion is no longer independent of each other due to the impenetrable condition, which makes it hard to derive a close-form expression of the probability function of each overlapping state $p(\xi_i)$. However, numerical experiments based on Monte-Carlo simulations could be employed to determined the probability functions in these complex models.

(iii) The inclusions can have a irregular shape, other than ellipse in 2-D and ellipsoid in 3-D. Due to a lack of analytical solutions for strain, the inclusion would need to discretized and a volume-integral would need to be employed to solve for the stain accurately. Hopefully, our proposed method reduces the need for discretizing complex inclusions because, complex geometries can be generated by overlapping inclusions with regular shapes.

## 6. Application to Polymer Nanocomposites

This section will discuss the interphase modeling of polymer nanocomposites. For this system, the inclusion is comprised of a spherical core particle (e.g., carbon or silicon nanoparticles) surrounded by an interphase region. As a result of the interaction between the polymer matrix and nanoparticles, the material properties in the interphase are different from those of the bulk polymer matrix material. The material properties are assumed uniform in the nanoparticle and interphase before any overlapping occurs. The stiffness tensor of the nanoparticle phase is $\mathbf{C}^{np}$, while the stiffness tensor of the interphase is $\mathbf{C}^{ip}$. The weighted-mean overlapping condition is chosen for the model. The weighting functions of the nanoparticle and interphase are denoted as $\eta^{np}$ and $\eta^{ip}$ respectively. Even if an interphase region overlaps with a particle, the particle properties should not be affected. To enforce this condition, $\eta^{np}$ is chosen to be much larger than $\eta^{ip}$,

$$\eta^{np} \gg \eta^{ip}. \tag{58}$$

The spacial distribution of the inclusions is chosen to follow the Poisson point process in Boolean-Poisson model. For these distributions, the aforementioned single phase model is first extended to two phases in Section 6.1 and then is applied to viscoelastic polymer composites in Section 6.

For linear viscoelastic materials, we use the complex modulus $E^*$ to represent the steady-state dynamic nature of the material,

$$E^*(i\omega) = E'(\omega) + iE''(\omega) = |E^*(i\omega)|e^{i\delta(\omega)}, \tag{59}$$

where $i$ is the imaginary unit that satisfy $i^2 = -1$, and $\omega$ is the angular velocity. The storage modulus is given by $E'$ and the loss modulus by $E''$. $E'$ and $E''$ are also called the dynamic moduli of the material. The phase lag between a steady oscillating stress and strain is $\delta(\omega)$. These values are related by

$$\tan\delta(\omega) = \frac{E''(\omega)}{E'(\omega)}. \tag{60}$$

### *6.1. Boolean-Poisson model with two-phase inclusions*

The volumes of the nanoparticle and interphase are denoted as $V^{np}$ and $V^{ip}$ respectively, with $V^{np}+V^{ip} = V^c$. As shown in Figure 8, the influence region with a center at the sampling point $\mathbf{x}_0$ can now be divided into a sphere with volume $V^{np}$ (region $B_0$) and a thick shell with volume $V^{ip}$ (region $B_1$). If the center of

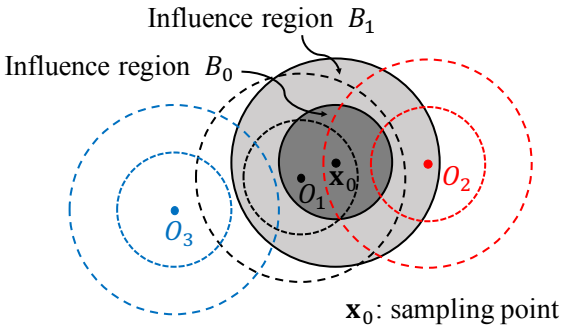


Figure 8: Illustration of the influence region $B_0$ centering at the sampling point $\mathbf{x}_0$. The center of the first inclusion $O_1$ is inside $B_0$, so that its nanoparticle phase overlaps with $\mathbf{x}_0$. While for the second inclusion, its center $O_2$ is inside $B_1$ so that its interphase overlaps with $\mathbf{x}_0$. For the third inclusion, its center $O_3$ is outside both $B_0$ and $B_1$ so that it will not influence the material properties at $\mathbf{x}_0$.

a inclusion is inside $B_0$, its nanoparticle phase will overlap with the sampling point. Because the weighting function of nanoparticle phase is much larger than that of the interphase, the corresponding stiffness tensor $\mathbf{C}_{(\xi_i)} = \mathbf{C}^{np}$ at the sampling point. If the center of the inclusion is inside $B_1$, its interphase will overlap with the sampling point. However, $\mathbf{C}_{(\xi_i)} = \mathbf{C}^{ip}$ only occurs when centers of all the other inclusions are outside $B_0$, and this state has a conditional probability equal to $e^{-\lambda V^{np}}$. Finally, if an inclusion center is neither in $B_0$ nor in $B_1$, the inclusion will not overlap with the sampling point and the properties at the sampling point will remain unaltered as the matrix material. By taking all the possible situations into account, we can divide the sampling space $\Xi$ into three subsets based on the material properties at the sampling point as shown in Figure 9. Set $\Xi_{ip}$ includes the states when $\mathbf{C}_{(\xi_i)} = \mathbf{C}^{ip}$, and Set $\Xi_{np}$ includes the states when $\mathbf{C}_{(\xi_i)} = \mathbf{C}^{np}$.

After calculating the probability function of each state using equation (36), the volume fractions of the nanoparticle phase $f_{np}$ and interphase $f_{ip}$ can be derived as

$$f_{np} = 1 - e^{-\lambda V^{np}}, \quad f_{ip} = e^{-\lambda V^{np}}\left[1 - e^{-\lambda V^{ip}}\right] \tag{61}$$

For mechanical properties, Eshelby's solution of spherical inclusion [18] and Tanaka-Mori's theorem [21] can be directly applied to model in Figure 9(b) and 9(c). However, due to the interphase effects, for the model in Figure 9(a), there exists no closed-form solution for inclusion strain, and strains in the nanoparticle phase and interphase become non-uniform. In this paper, we adopt the assumption in [34] that the strains are uniform in the nanoparticle and interphase, so that Eshelby's solution is applicable. While this assumption looses some accuracy in representing the spatial variation of strain in inclusions, we believe that these

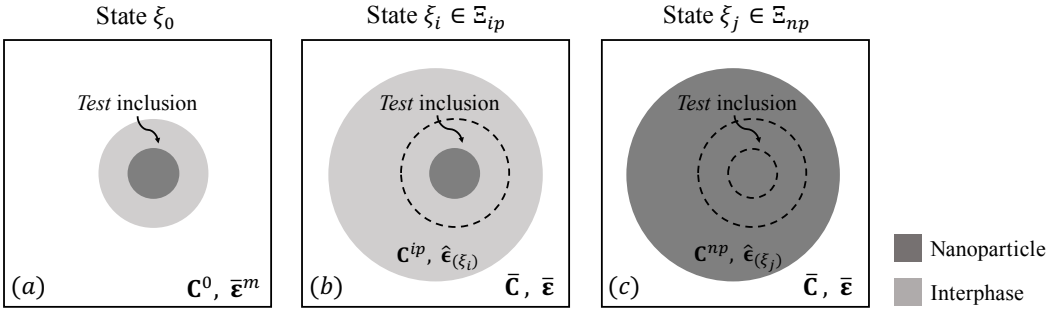


Figure 9: Illustration of the physical models of the two-phase inclusion under different overlapping states: (a) In state $\xi_0$, the *test* inclusion is embedded into the matrix material with stiffness tensor $\mathbf{C}^0$ and strain $\bar{\boldsymbol{\varepsilon}}^m$; (b) In state $\xi_i \in \Xi_{ip}$, the *test* inclusion in embedded into an overlapping region with the interphase's stiffness tensor $\mathbf{C}^{ip}$ and strain $\hat{\boldsymbol{\epsilon}}_{(\xi_i)}$; (c) In state $\xi_j \in \Xi_{np}$, the *test* inclusion in embedded into an overlapping region with the nanoparticle's stiffness tensor $\mathbf{C}^{np}$ and strain $\boldsymbol{\varepsilon}_{(\xi_j)}$.

spatial variations should have a minor effect of the effective properties. However, if these spatial variations are needed, the inclusion could be discretized as in [25]. By taking all overlapping states into account, we can get the expected values of the strain $\langle \boldsymbol{\varepsilon}_{np}^{\text{test}} \rangle$ in the nanoparticle phase and $\langle \boldsymbol{\varepsilon}_{ip}^{\text{test}} \rangle$ in the interphase of the test inclusion (see equation (A.1) and (A.2)). In order to close the scheme, the equations of average strain and stress are needed, which are given as

$$\bar{\boldsymbol{\varepsilon}} = (1 - f_{np} - f_{ip})\bar{\boldsymbol{\varepsilon}}^m + \lambda \left( V^{np} \langle \boldsymbol{\varepsilon}_{np}^{\text{test}} \rangle + V^{ip} \langle \boldsymbol{\varepsilon}_{ip}^{\text{test}} \rangle \right), \tag{62}$$

and

$$\bar{\boldsymbol{\sigma}} = \mathbf{C}^0 : \bar{\boldsymbol{\varepsilon}} + \lambda \left( V^{np} \delta \mathbf{C}^{np} : \langle \boldsymbol{\varepsilon}_{np}^{\text{test}} \rangle + V^{ip} \delta \mathbf{C}^{ip} : \langle \boldsymbol{\varepsilon}_{ip}^{\text{test}} \rangle \right), \tag{63}$$

where $\langle \boldsymbol{\varepsilon}^{np} \rangle$ and $\langle \boldsymbol{\varepsilon}^{ip} \rangle$ are the expectations of strain in the nanoparticle phase and interphase respectively. Finally the effective stiffness tensor $\bar{\mathbf{C}}$ of the Boolean-Poisson model with two-phase inclusions can be expressed as

$$\bar{\mathbf{C}} = \mathbf{C}^0 + \lambda \left( V^{np} \delta \mathbf{C}^{np} : \langle \mathbf{A}^{np} \rangle + V^{ip} \delta \mathbf{C}^{ip} : \langle \mathbf{A}^{ip} \rangle \right), \tag{64}$$

where $\langle \mathbf{A}^{np} \rangle$ and $\langle \mathbf{A}^{ip} \rangle$ are defined in equation (A.8). More detailed derivations are provided in Appendix A.

### *6.2. Inverse modeling of interphase properties*

Next, we will demonstrate how to combine our micromechanics model with experiment data from a composite to approximate the interphase properties in 3-D. We use the experimental data of carbon-black filled styrene butadiene rubbers with various volume fractions of fillers (0%, 2.4%, 13.0%, 16.7%, 20.0% and 23.0%) from Diani's paper [27], where 0% filler represents the matrix properties. Dynamic mechanical analysis (DMA) was used to experimentally characterize the linear viscoelasticity of each material, and the master curves of the storage modulus $E'$ and loss modulus $E''$ were reconstructed at a reference temperature 0°C. The matrix and interphase are considered nearly incompressible with Poisson's ratios of $\nu_0 = 0.499$ and $\nu_{ip} = 0.499$ respectively. The Young's modulus and Poisson's ratio of the nanoparticle material (carbon-black) are $E_{np} = 30$ GPa and $\nu_{np} = 0.19$ respectively. The complex modulus and thickness of the interphase are assumed to be independent of the volume fraction of nanoparticles.

A flowchart describing the inverse modeling of interphase properties is provided in Figure 10. For a given interphase thickness $d_{ip}$, together with the known properties of the matrix and nanoparticle materials, the effective complex modulus of a simulated composite $E^*_{\text{simulated}}$ is only a function of the interphase's complex modulus $E^*_{ip}$, based on equation (64). As shown in the "Optimization" box, the objective is to find the optimum interphase complex modulus that minimizes the difference between the simulated effective modulus $E^*_{\text{simulated}}(E^*_{ip})$ and the experimentally measured value $E^*_{expt}$ for the same composite material. Since

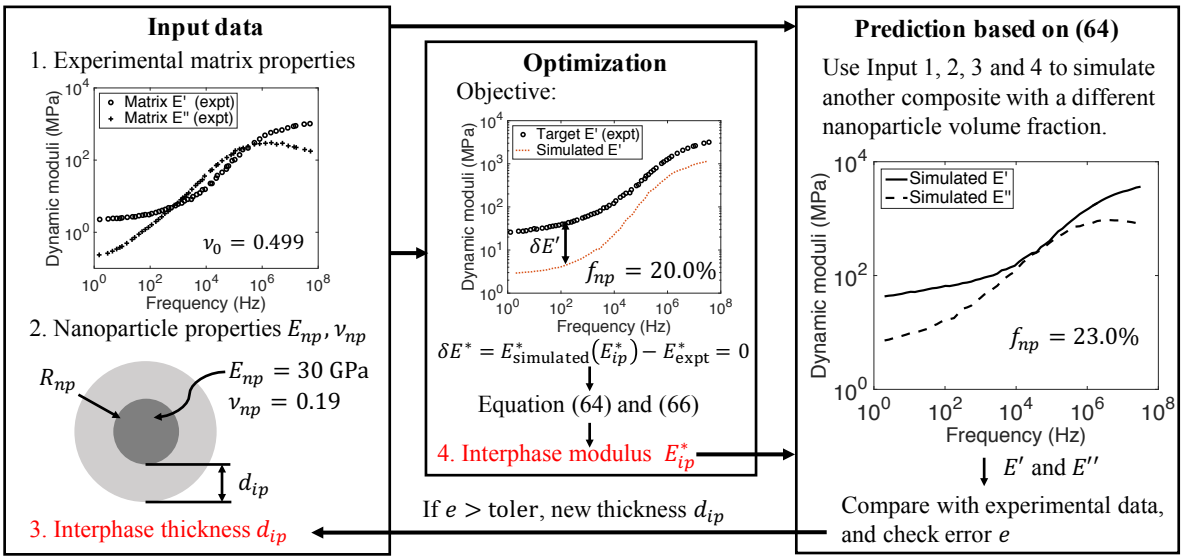


Figure 10: Flowchart summarizing the inverse modeling of interphase properties based on the extended micromechanics method developed in this work. The interphase properties are assumed to be independent of the amount of fillers.

no constraint is put on the interphase properties in our current work, the optimization problem becomes a root-finding exercise, which solves for $E^*_{ip}$ such that

$$\delta E^* = E^*_{\text{simulated}}(E^*_{ip}) - E^*_{expt} = 0 \quad \text{at each frequency point.} \tag{65}$$

The experimental data for nanoparticle volume fraction 20% is chosen as the reference for $E^*_{expt}$. In order to solve equation (65), we use the secant method to search for the complex modulus of the interphase at every frequency point. The recurrence relation using the secant method can be written as

$$E^*_{ip}[n] = E^*_{ip}[n-1] - \delta E^*[n-1]\frac{E^*_{ip}[n-1] - E^*_{ip}[n-2]}{\delta E^*[n-1] - \delta E^*[n-2]}, \tag{66}$$

where $n$ denotes the iteration number. We will continue this process until we reach a sufficiently high level of accuracy with respect to the experimental results for the composite modulus. After obtaining the interphase modulus $E^*_{ip}$, we can calculate the effective properties of another composite with a different amount of fillers (specifically we compare to a volume fraction 23%). By comparing these predictions with experimental data, we can evaluate whether the choice of the interphase thickness ($d_{ip}$) is physical.

Using the procedure in Figure 10, the interphase thickness ($d_{ip}$) is found to be in the range

$$d_{ip} = 0.60R_{np} \quad \text{to} \quad 0.65R_{np}, \tag{67}$$

which gives converged interphase modulus, as well as accurate predictions of the effective dynamic moduli within the whole frequency range ($1 - 10^8$ Hz). For typical nanoparticles with radius $R_{np} = 30$ nm, the interphase thickness is around $18-20$ nm, which is realistic according to AFM nano-indentation experiments in [9]. In this section, we will show the results for $d_{ip} = 0.62R_{np}$.

The predicted dynamic moduli of the interphase are shown in Figure 11 together with those of the matrix material. As we can see from the figure, the dynamic moduli of the interphase is higher than the dynamic moduli of the matrix across the whole frequency range due to the presence of polymer-nanoparticle interaction. Also the ratio of interphase dynamic moduli to the dynamic moduli of bulk matrix is larger in the lower frequency (higher temperature) domain indicating a stronger effect of polymer-nanoparticle interaction.

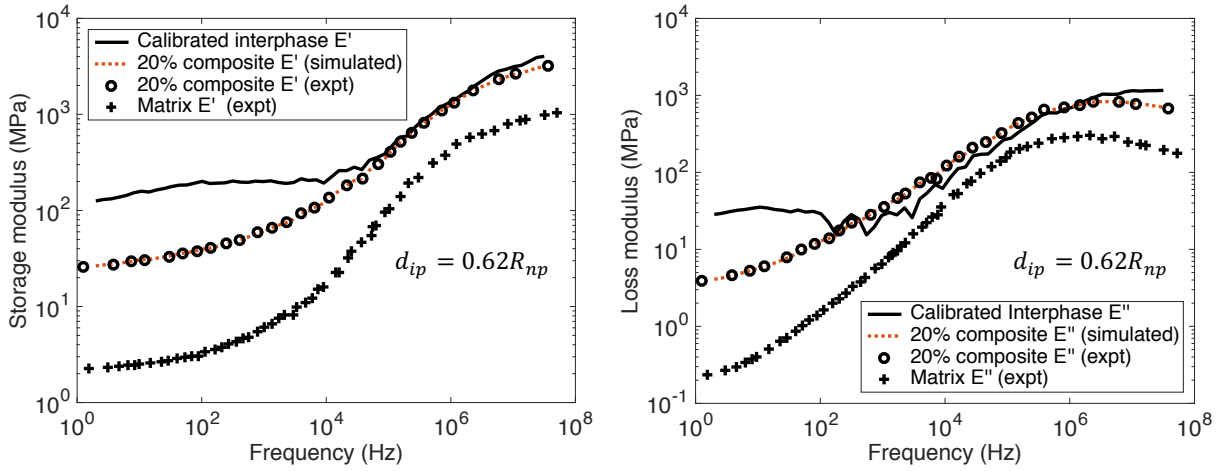


Figure 11: Predicted interphase's storage modulus (Left) and loss modulus (Right) based on the experimental data of nanoparticle volume fraction 20.0% and $d_{ip} = 0.62R_{np}$.The matrix (plus) and interphase (solid line) are composed of the same materials but have noticeably different mechanical responses.

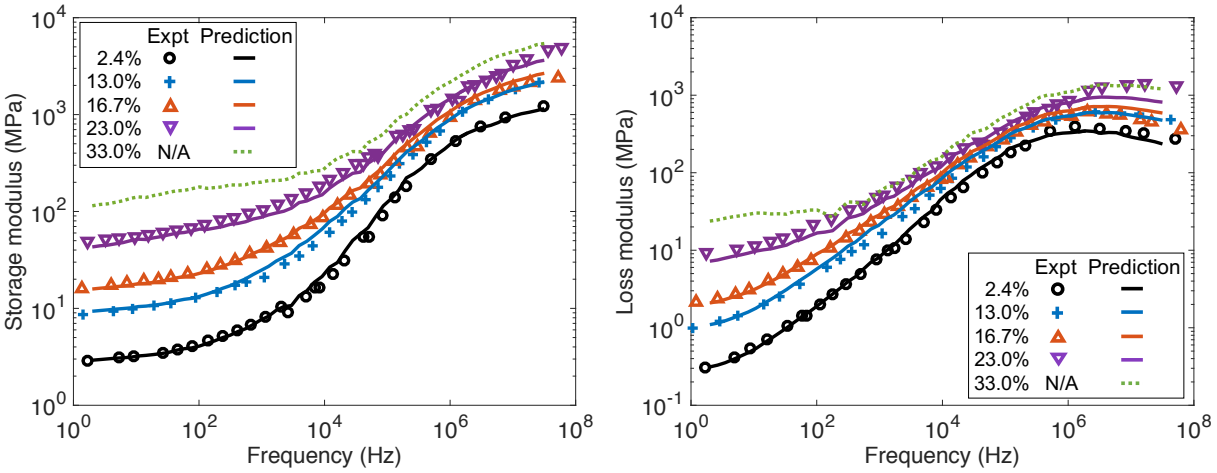


Figure 12: Experimental validation of the inversely predicted interphase properties for nanoparticle volume fraction 2.4%, 13.0% and 16.7%. The solid lines are the predicted dynamic moduli based on the interphase properties shown in Figure 11 with thickness $d_{ip} = 0.62R_{np}$. Predictions for nanoparticle volume fraction 23% and 33.0% are also provided for comparison.

Furthermore, the predicted dynamic moduli and the choice of the interphase thickness are validated against experimental data with nanoparticle volume fraction 2.4%, 13.0% and 16.7%. As we can see from Figure 12, the experimental data agrees well with the predictions of the extended micromechanics method across the whole frequency range. Since our model's interphase properties and thickness were predicted with one set of filler volume fractions (20% and 23%) and – using these interphase properties – the model showed agreement for a different set of volume fractions (2.4%, 13.0% and 16.7%), it is suggested by our proposed method that the amount of nanoparticles has little influence on interphase properties.

## 7. Conclusion

This paper proposed a new mathematical framework of overlapping geometries that allows for the study of dilute particles, clustered particles and interacting interphases in polymer nanocomposites. Weighted-

mean and additive overlapping conditions were introduced to consider various physical phenomena in the overlapping regions. The corresponding inclusion-wise strain definitions and integral equations under these two overlapping conditions were derived. This framework was applied to linear elastic clusters of particles as well as viscoelastic materials with interphases. Using a Boolean-Poisson model, DNS results under both weighted-mean and additive overlapping conditions were well captured by the proposed method. The method was also capable of capturing the effect of various distributions of inclusions, while the Mori-Tanaka and self-consistent methods depend only on volume fraction of the overall inclusion phase. Finally, the proposed method was applied to a viscoelastic of polymer nanocomposite with an interphase region (i.e., carbon-black filled styrene butadiene rubbers system) . The inversely predicted interphase properties, including interphase thickness and complex modulus,were further validated by experimental data. For reinforcing particles with radius of 30 nm, the thickness of the interphase region was found to be around $18-20$ nm. The model also suggested that interphase properties may be independent of filler volume fraction for the system studied.

The methods presented above rely on the general assumption of linear material behavior. While extensions to non-linear material behavior is not explored here, the methods of Pedro Ponte Castaeda (nonlinear bounds [35], second-order estimation of nonlinear phase potential [36]), and George J. Dvorak (transformation field analysis [37]) seem to be the most promising areas for extension of this work to non-linear regimes. However, despite the linear modeling limitation, the range of applications for the present work is still large, due to the extensive challenge of representing RVE scale elastic properties based on complex nanoscale morphologies, and the broad applications of viscoelastic materials ranging in scale from consumer goods [4] to civil engineering [38].


## Acknowledgement

Z.L. and W.K.L. warmly thank the support from AFOSR grant No. FA9550-14-1-0032. Z.L. would like to thank Stephen Lin and Benjamin Sonin for their parts in helpful discussions. This work performed, in part, under the auspices of the U.S. Department of Energy by Lawrence Livermore National Laboratory under Contract DE-AC52-07NA27344 (LLNL-JRNL-673797).


## Appendix A. Expectation of strains in Boolean-Poisson model with two-phase inclusions

By taking all overlapping states shown in Figure 9 into account and using equation 61 of volume fraction $f_{np}$ and $f_{ip}$, we can calculate the expected values of the strain $\langle \boldsymbol{\varepsilon}_{np}^{\text{test}} \rangle$ in the nanoparticle phase and $\langle \boldsymbol{\varepsilon}_{ip}^{\text{test}} \rangle$ in the interphase of the test inclusion as

$$\langle \boldsymbol{\varepsilon}_{np}^{\text{test}} \rangle = (1 - f_{np} - f_{ip}) \mathbf{T}_{(\xi_0)}^{np} : \bar{\boldsymbol{\varepsilon}}^m + f_{ip} \mathbf{T}_{(\xi_i)}^{np} : \mathbf{A}^{ip} : \bar{\boldsymbol{\varepsilon}} + \left( \frac{f_{np}}{\lambda V^{np}} - e^{\lambda V^{np}} \right) \mathbf{A}^{np} : \bar{\boldsymbol{\varepsilon}} \tag{A.1}$$

and

$$\langle \boldsymbol{\varepsilon}_{ip}^{\text{test}} \rangle = (1 - f_{np} - f_{ip}) \mathbf{T}_{(\xi_0)}^{ip} : \bar{\boldsymbol{\varepsilon}}^m + \left( \frac{f_{ip}}{\lambda V^{ip}} - e^{\lambda (V^{np} + V^{ip})} \right) : \mathbf{A}^{ip} : \bar{\boldsymbol{\varepsilon}}, \tag{A.2}$$

where $\lambda$ is the rate of the stationary Poisson point process in the Boolean-Poisson model (see Section 5.2). Also, $V^{np}$ and $V^{ip}$ denote the volumes of the nanoparticle phase and the interphase in each inclusion. The concentration tensors $\mathbf{T}$ in the *test* inclusion are

$$\mathbf{T}_{(\xi_0)}^{np} = \left[ \mathbf{I} + \mathbf{S}^0 : (\mathbf{C}^0)^{-1} : (\mathbf{C}^{np} - \mathbf{C}^0) \right]^{-1}, \quad \mathbf{T}_{(\xi_i)}^{np} = \left[ \mathbf{I} + \mathbf{S}^{ip} : (\mathbf{C}^{ip})^{-1} : (\mathbf{C}^{np} - \mathbf{C}^{ip}) \right]^{-1} \tag{A.3}$$

and

$$\mathbf{T}_{(\xi_0)}^{ip} = \left[ \mathbf{I} + \mathbf{S}^0 : (\mathbf{C}^0)^{-1} : (\mathbf{C}^{ip} - \mathbf{C}^0) \right]^{-1}. \tag{A.4}$$

The strain concentration tensors $\mathbf{A}$ of the nanoparticle and interphase materials are related to the properties of the effective medium,

$$\mathbf{A}^{np} = \left[ \mathbf{I} + \bar{\mathbf{S}} : (\bar{\mathbf{C}}^{-1} : (\mathbf{C}^{np} - \bar{\mathbf{C}}) \right]^{-1} \quad \text{and} \quad \mathbf{A}^{ip} = \left[ \mathbf{I} + \bar{\mathbf{S}} : (\bar{\mathbf{C}}^{-1} : (\mathbf{C}^{ip} - \bar{\mathbf{C}}) \right]^{-1}. \tag{A.5}$$

According to the consistent equation (62), the average strain in the matrix can be written as

$$(1 - f_{np} - f_{ip})\bar{\boldsymbol{\varepsilon}}^m = \bar{\boldsymbol{\varepsilon}} - \lambda \left( V^{np} \langle \boldsymbol{\varepsilon}_{np}^{\text{test}} \rangle + V^{ip} \langle \boldsymbol{\varepsilon}_{ip}^{\text{test}} \rangle \right), \tag{A.6}$$

By substituting equation (A.1) into (A.2) and (A.6 and rearranging the fomulation, we obtain the system of equations for solving $\langle \boldsymbol{\varepsilon}_{np}^{\text{test}} \rangle$ and $\langle \boldsymbol{\varepsilon}_{ip}^{\text{test}} \rangle$,

$$\begin{bmatrix} \mathbf{I} + \lambda V^{np} \mathbf{T}_{(\xi_0)}^{np} & \lambda V^{ip} \mathbf{T}_{(\xi_0)}^{np} \\ \lambda V^{np} \mathbf{T}_{(\xi_0)}^{ip} & \mathbf{I} + \lambda V^{ip} \mathbf{T}_{(\xi_0)}^{ip} \end{bmatrix} \begin{bmatrix} \langle \boldsymbol{\varepsilon}_{np}^{\text{test}} \rangle \\ \langle \boldsymbol{\varepsilon}_{ip}^{\text{test}} \rangle \end{bmatrix} = \begin{bmatrix} \mathbf{T}_{(\xi_0)}^{np} + f_{ip} \mathbf{T}_{(\xi_i)}^{np} : \mathbf{A}^{ip} + \left( \dfrac{f_{np}}{\lambda V^{np}} - e^{\lambda V^{np}} \right) \mathbf{A}^{np} \\ \mathbf{T}_{(\xi_0)}^{ip} + \left( \dfrac{f_{ip}}{\lambda V^{ip}} - e^{\lambda (V^{np} + V^{ip})} \right) : \mathbf{A}^{ip} \end{bmatrix} \bar{\boldsymbol{\varepsilon}} \tag{A.7}$$

Finally the expected values of strain in the *test* inclusioin can be solved as a function of the average strain $\bar{\boldsymbol{\varepsilon}}$ based on equation (A.7),

$$\langle \boldsymbol{\varepsilon}_{np}^{\text{test}} \rangle = \langle \mathbf{A}^{np} \rangle : \bar{\boldsymbol{\varepsilon}} \quad \text{and} \quad \langle \boldsymbol{\varepsilon}_{ip}^{\text{test}} \rangle = \langle \mathbf{A}^{ip} \rangle : \bar{\boldsymbol{\varepsilon}} \tag{A.8}$$

## References


[1] A. C. Balazs, T. Emrick, T. P. Russell, Nanoparticle polymer composites: where two small worlds meet, Science 314 (5802) (2006) 1107–1110.

[2] T. Ramanathan, A. Abdala, S. Stankovich, D. Dikin, M. Herrera-Alonso, R. Piner, D. Adamson, H. Schniepp, X. Chen, R. Ruoff, et al., Functionalized graphene sheets for polymer nanocomposites, Nature nanotechnology 3 (6) (2008) 327–331.

[3] R. Qiao, L. C. Brinson, Simulation of interphase percolation and gradients in polymer nanocomposites, Composites Science and Technology 69 (3) (2009) 491–499.

[4] M.-J. Wang, Effect of polymer-filler and filler-filler interactions on dynamic properties of filled vulcanizates, Rubber Chemistry and Technology 71 (3) (1998) 520–589.

[5] V. N. Mochalin, O. Shenderova, D. Ho, Y. Gogotsi, The properties and applications of nanodiamonds, Nature nanotechnology 7 (1) (2012) 11–23.

[6] C. J. Ellison, J. M. Torkelson, The distribution of glass-transition temperatures in nanoscopically confined glass formers, Nature Materials 2 (10) (2003) 695–700.

[7] S. Watcharotone, C. D. Wood, R. Friedrich, X. Chen, R. Qiao, K. Putz, L. C. Brinson, Interfacial and substrate effects on local elastic properties of polymers using coupled experiments and modeling of nanoindentation, Advanced Engineering Materials 13 (5) (2011) 400–404.

[8] Y. Li, M. Kröger, W. K. Liu, Nanoparticle effect on the dynamics of polymer chains and their entanglement network, Physical review letters 109 (11) (2012) 118001.

[9] X. Cheng, K. W. Putz, C. D. Wood, L. C. Brinson, Characterization of local elastic modulus in confined polymer films via afm indentation, Macromolecular rapid communications 36 (2014) 391–397.

[10] R. Peng, H. Zhou, H. Wang, L. Mishnaevsky, Modeling of nano-reinforced polymer composites: Microstructure effect on youngs modulus, Computational Materials Science 60 (2012) 19–31.

[11] H. Moulinec, P. Suquet, A numerical method for computing the overall response of nonlinear composites with complex microstructure, Computer methods in applied mechanics and engineering 157 (1) (1998) 69–94.

[12] H. Moulinec, P. Suquet, Comparison of fft-based methods for computing the response of composites with highly contrasted mechanical properties, Physica B: Condensed Matter 338 (1) (2003) 58–60.

[13] Z. Hashin, The elastic moduli of heterogeneous materials, Journal of Applied Mechanics 29 (1) (1962) 143–150.

[14] Z. Hashin, S. Shtrikman, A variational approach to the theory of the elastic behaviour of multiphase materials, Journal of the Mechanics and Physics of Solids 11 (2) (1963) 127–140.

[15] Z. Hashin, B. W. Rosen, The elastic moduli of fiber-reinforced materials, Journal of applied mechanics 31 (2) (1964) 223–232.

[16] G. Milton, Bounds on the elastic and transport properties of two-component composites, Journal of the Mechanics and Physics of Solids 30 (3) (1982) 177–191.

[17] S. Torquato, Random heterogeneous media: microstructure and improved bounds on effective properties, Applied mechanics reviews 44 (2) (1991) 37–76.

[18] J. D. Eshelby, The determination of the elastic field of an ellipsoidal inclusion, and related problems, in: Proceedings of the Royal Society of London A: Mathematical, Physical and Engineering Sciences, Vol. 241, The Royal Society, 1957, pp. 376–396.

[19] T. Mori, K. Tanaka, Average stress in matrix and average elastic energy of materials with misfitting inclusions, Acta metallurgica 21 (5) (1973) 571–574.

[20] R. Hill, A self-consistent mechanics of composite materials, Journal of the Mechanics and Physics of Solids 13 (4) (1965) 213–222.

[21] T. Mura, Micromechanics of defects in solids, Vol. 3, Springer Science & Business Media, 1987.

[22] R. Christensen, K. Lo, Solutions for effective shear properties in three phase sphere and cylinder models, Journal of the Mechanics and Physics of Solids 27 (4) (1979) 315–330.
[23] H. Liu, L. C. Brinson, Reinforcing efficiency of nanoparticles: a simple comparison for polymer nanocomposites, Composites Science and Technology 68 (6) (2008) 1502–1512.
[24] J. Diani, P. Gilormini, Using a pattern-based homogenization scheme for modeling the linear viscoelasticity of nano-reinforced polymers with an interphase, Journal of the Mechanics and Physics of Solids 63 (2014) 51–61.
[25] Z. Liu, J. A. Moore, S. M. Aldousari, H. S. Hedia, S. A. Asiri, W. K. Liu, A statistical descriptor based volume-integral micromechanics model of heterogeneous material with arbitrary inclusion shape, Computational Mechanics (2015) 1–19.
[26] Z. Liu, A. M. Bessa, W. K. Liu, Self-consistent clustering analysis: an efficient multi-scale scheme for inelastic heterogeneous materials, Computer Methods in Applied Mechanics and Engineering.
[27] J. Diani, P. Gilormini, Y. Merckel, F. Vion-Loisel, Micromechanical modeling of the linear viscoelasticity of carbon-black filled styrene butadiene rubbers: The role of the filler–rubber interphase, Mechanics of Materials 59 (2013) 65–72.
[28] M. Haenggi, J. G. Andrews, F. Baccelli, O. Dousse, M. Franceschetti, Stochastic geometry and random graphs for the analysis and design of wireless networks, Selected Areas in Communications, IEEE Journal on 27 (7) (2009) 1029–1046.
[29] A. Jean, D. Jeulin, S. Forest, S. Cantournet, F. N'GUYEN, A multiscale microstructure model of carbon black distribution in rubber, Journal of microscopy 241 (3) (2011) 243–260.
[30] S. Torquato, Effective stiffness tensor of composite mediai. exact series expansions, Journal of the Mechanics and Physics of Solids 45 (9) (1997) 1421–1448.
[31] Y. Benveniste, A new approach to the application of mori-tanaka's theory in composite materials, Mechanics of materials 6 (2) (1987) 147–157.
[32] S. N. Chiu, D. Stoyan, W. S. Kendall, J. Mecke, Stochastic geometry and its applications, John Wiley & Sons, 2013.
[33] S. Torquato, Random heterogeneous materials: microstructure and macroscopic properties, Vol. 16, Springer Science & Business Media, 2013.
[34] S. Nemat-Nasser, M. Hori, Micromechanics: overall properties of heterogeneous materials, Elsevier, 2013.
[35] P. P. Castañeda, The effective mechanical properties of nonlinear isotropic composites, Journal of the Mechanics and Physics of Solids 39 (1) (1991) 45–71.
[36] P. P. Castañeda, Second-order homogenization estimates for nonlinear composites incorporating field fluctuations: Itheory, Journal of the Mechanics and Physics of Solids 50 (4) (2002) 737–757.
[37] G. J. Dvorak, Transformation field analysis of inelastic composite materials, in: Proceedings of the Royal Society of London A: Mathematical, Physical and Engineering Sciences, Vol. 437, The Royal Society, 1992, pp. 311–327.
[38] C. W. Roeder, J. F. Stanton, Elastomeric bearings: state-of-the-art, Journal of Structural Engineering 109 (12) (1983) 2853–2871.